https://doi.org/10.5194/egusphere-2026-1739
Preprint. Discussion started: 20 May 2026

Role of Low-Level Jet Evolution in Vertical Aerosol Redistribution: A Doppler Wind Lidar Study Over East China

Tianle Bai, Yuanyi Lin, Mengya Wang, Tianwen Wei, Fangzhi Wei, Kuancheng Lv, Haiyun Xia

The State Key Laboratory of Climate System Prediction and Risk Management (CPRM), School of Atmospheric Physics, Nanjing University of Information Science & Technology, Nanjing, 210044, China

Correspondence to: Mengya Wang (wmengya123@nuist.edu.cn)

Abstract. Low-level jets (LLJs) significantly influence aerosol vertical transport and the resulting surface air quality. This study utilizes coherent Doppler wind lidar observations to characterize the impact of LLJ dynamics on vertical aerosol redistribution during two typical dust episodes over Hefei, East China. Results show that the vertical trajectory of the LLJ core is associated with dust transport through the combined effects of mechanical shear and thermal stability. In the April 2021 event, the northwesterly jet core exhibits a dynamic vertical evolution, descending from 2.5 km to 0.3 km before re-ascending to 1.0 km by the time of the surface PM_{10} peak (410 μg m^{-3}). This movement maintains enhanced wind shear (> 0.04 s^{-1}) and associated mechanical turbulence at the jet's lower interface. Together, these processes are associated with the downward transport of dust into the surface layer through vertical coupling at the frontal leading edge. This corresponds to a surface PM_{10} peak with little temporal delay relative to the onset of frontal influence. Conversely, the March 2022 event is characterized by a relatively stable LLJ core and a persistent capping inversion that acts as a structural barrier, maintaining the dust layer aloft. Persistent wind shear and turbulence below the jet core are associated with sustained elevated transport and temporary aerosol storage prior to the delayed surface response. This configuration decouples the LLJ from the surface, resulting in an approximately 8-hour phase lag between the onset of the surface frontal influence and the PM_{10} peak (578 μg m^{-3}). The peak occurs during the transient breakdown of the capping inversion, coinciding with the downward redistribution of the elevated aerosol layer. Wind hodographs indicate that inertial oscillations contribute to the maintenance of these dust-laden LLJs following frictional decoupling. Overall, LLJ evolution is associated with either rapid downward redistribution or elevated storage with delayed surface release, depending on the jet height relative to boundary-layer stability. The results provide an observational basis for refining boundary-layer parameterizations in numerical weather prediction and air quality models.

1 Introduction

Aerosols play an important role in the Earth's radiation budget and climate system through their scattering and absorption of solar radiation (Kok et al., 2023; Li et al., 2019, 2016). Beyond radiative effects, interactions between aerosols and boundary-layer processes critically influence air quality and public health (Li et al., 2017; Pöschl, 2005), particularly

https://doi.org/10.5194/egusphere-2026-1739
Preprint. Discussion started: 20 May 2026

during pollution episodes when downward transport and vertical confinement enhance surface concentrations (Guo et al., 2016; Tian et al., 2017). In East China, a region frequently affected by transboundary aerosol transport (Huang et al., 2020; Qin et al., 2016), stratified aerosol structures are shaped by the combined influence of large-scale synoptic circulation and boundary-layer dynamical processes (Chen et al., 2018; Zheng et al., 2015). However, direct observational evidence on the high-frequency response of aerosol layering to the rapid structural evolution of wind fields remains limited.

Among these processes, low-level jets (LLJs) are localized wind maxima in the lower troposphere that play an important role in regional-scale pollutant transport and boundary-layer regulation (Sullivan et al., 2017; Wei et al., 2023; Wu et al., 2020; Zhang et al., 2001). LLJs also influence regional climate through their control on the horizontal and vertical redistribution of heat and moisture and their role in modulating deep convective activity (Stensrud, 1996). In addition to horizontal advection, the persistent vertical wind shear associated with LLJs provides a continuous source of mechanical turbulence, which significantly alters the vertical structure of the lower atmosphere (Gutierrez et al., 2017; Yang et al., 2023). However, these effects are not a simple linear response to wind speed or shear magnitude but depend on the continuous evolution of the jet's vertical position and intensity as well as concurrent changes in atmospheric stability (Banta et al., 2002; Mahrt, 1998). Consequently, the lifecycle of jet structures is closely associated with changes in aerosol vertical distribution, highlighting the need to examine the concurrent evolution of wind profiles and aerosol stratification.

Within this framework, the influence of LLJs on aerosol vertical redistribution may be interpreted through two interconnected pathways. One pathway is dynamical, whereby episodic shear-generated turbulence during the formation, intensification, or decay of an LLJ promotes the downward mixing of elevated aerosol layers (Heinold et al., 2015, 2013). The other pathway is structural, in which the shifting vertical position of the jet core modulates boundary-layer depth and stability, thereby regulating the vertical placement and confinement of aerosol layers (Su et al., 2020; Wang et al., 2019). Despite this conceptual understanding, how these pathways interact under rapidly evolving LLJ conditions remains poorly constrained. In particular, the timing and vertical coherence between jet evolution, turbulence generation, and aerosol layer adjustment in the lower troposphere are not yet well resolved, limiting a process-level interpretation of aerosol vertical redistribution and its implications for near-surface pollution.

To investigate the dynamical and structural pathways associated with LLJ-related aerosol redistribution, observational tools capable of resolving both wind-field evolution and aerosol layering at high temporal and vertical resolution are essential. Coherent Doppler wind lidar (CDWL) provides this capability by simultaneously measuring wind profiles, vertical wind shear, turbulence intensity, and aerosol backscatter with fine spatiotemporal resolution (Banakh et al., 2017; Frehlich, 1994; Wang et al., 2024; Wei et al., 2025a). These measurements allow for the assessment of how the evolution of LLJ structures, including their formation, descent, intensification, and decay, is associated with changes in aerosol vertical distribution (Andújar-Maqueda et al., 2026; Beu and Landulfo, 2022; Wei et al., 2025b). Previous lidar-based studies have primarily documented the vertical structure and temporal variability of LLJs or identified elevated aerosol layers associated with synoptic-scale transport during specific events (Andújar-Maqueda et al., 2026; Dieudonné et al., 2023; Huang et al.,

https://doi.org/10.5194/egusphere-2026-1739
Preprint. Discussion started: 20 May 2026

2021; Iwai et al., 2011; Tuononen et al., 2017; Yang et al., 2019). However, how aerosol vertical structure adjusts to the rapid evolution of LLJ dynamics at the event scale remains insufficiently explored.

In this study, we investigate the role of LLJ evolution in vertical aerosol redistribution using coherent Doppler wind lidar observations over Hefei, East China. Two dust transport events with distinct dynamical characteristics are analyzed: an April 2021 episode featuring vertical migration of the jet core, and a March 2022 episode characterized by a more stable, elevated jet structure. By integrating synoptic analyses, high-resolution lidar measurements, and surface air quality observations, this study aims to characterize the vertical response of aerosol stratification to the LLJ evolution and examine how this dynamical adjustment is associated with the development of near-surface pollution.

2 Data and methodology

2.1 Study area and instrument

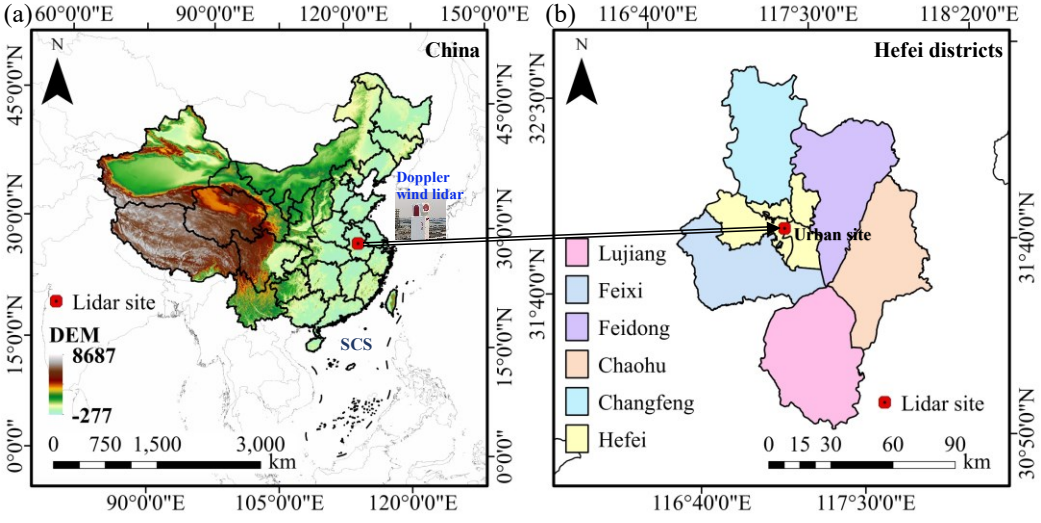

Figure 1. Overview of the study area and observational site: (a) Topographic map of China indicating the location of the coherent Doppler wind lidar (CDWL) station in Hefei; (b) Administrative map of Hefei districts, with the red dot marking the specific urban site where the CDWL measurements are conducted. The color-coded areas in (b) represent the distinct administrative subdivisions of Hefei.

Hefei (Fig. 1a) is situated on the Jiang-Huai Plain in East China, occupying a transitional location between the Yangtze and Huaihe River basins. The topography is characterized by flat and low-lying terrain, with elevations ranging from 15 to 80 m (Zhao and Zou, 2018). The region is governed by a humid subtropical monsoon climate, which serves as a climatic transition zone between northern and southern China. This positioning results in distinct seasonal variations, with an annual precipitation of approximately 1000 mm concentrated during the summer months (Wang et al., 2023).

Given its location downwind of major East Asian dust sources, Hefei is frequently affected by the long-range transport of mineral dust from the Gobi and Taklamakan Deserts, particularly during the spring transition (Zhou et al., 2002). The low

https://doi.org/10.5194/egusphere-2026-1739
Preprint. Discussion started: 20 May 2026

surface roughness of the expansive plain facilitates the frequent development of LLJs, which are a prominent feature of the nocturnal boundary layer in this region. Furthermore, the rapid expansion of the Hefei metropolitan area has intensified the local anthropogenic emissions, primarily from transportation and industrial activities (Zhou et al., 2021). During dust events, the interaction between these local pollutants and descending dust layers leads to complex aerosol stratification (Wang et al., 2022). Consequently, the integration of these geographical and meteorological factors makes the city well-suited for investigating the fine-scale response of aerosol vertical redistribution to LLJ dynamics.

The CDWL system (Fig. 1b) is installed on the roof of the School of Earth and Space Science building at the University of Science and Technology of China (31.83°N, 117.25°E) in Hefei. It is utilized to measure vertical profiles of the aerosol backscatter coefficient and wind field with high spatiotemporal resolution. The system operates at an eye-safe wavelength of 1.5 μm and emits pulses of 300 μJ at a 10 kHz repetition rate, providing a maximum detection range of 15 km. To derive three-dimensional wind vectors (Banakh et al., 2010; Smalikho, 2003), the CDWL employs a velocity azimuth display (VAD) scanning mode at a constant elevation angle of 60°. The azimuth angle ranges from 0° to 300° with an interval of 5°. Under this scanning geometry, the horizontal wind direction increases clockwise (0° for true north), and negative vertical velocities denote updrafts. Detailed information and validation of the CDWL can be found in previous studies (Jia et al., 2019; Wei et al., 2020, 2019).

2.2 Doppler lidar parameter retrieval

To ensure the reliability of the retrieved wind and aerosol profiles, a rigorous quality control (QC) procedure is implemented. First, a carrier-to-noise ratio (CNR) threshold of -28 dB is applied to remove signals dominated by background noise while retaining the continuity of aerosol and wind structures in the lower troposphere. The retrieved profiles are further visually examined for temporal continuity across neighboring range gates in order to minimize contamination from transient hard targets and isolated noisy bins. Second, a continuity check is performed on the vertical velocity and horizontal wind vectors to identify and remove outliers caused by transient hard targets (e.g., birds or aircraft) or extreme atmospheric turbulence.

The attenuated aerosol backscatter coefficient (β) is retrieved from the CNR using a semi-qualitative calibration method (Huang et al., 2021; Pentikäinen et al., 2020; Wei et al., 2022). The calculation is expressed as:

$$\beta(r) = C\frac{CNR(r) * r^2}{T_f(r)} \quad (1)$$

where r denotes the range, C refers to a calibration factor determined by integrating backscattered signals from optically thick, non-drizzling stratocumulus clouds (O'Connor et al., 2004). $T_f(r)$ represents the focus function, which is derived from horizontal scans assuming a homogeneous aerosol distribution (Yang et al., 2020).

Vertical wind shear (S) is calculated as the magnitude of the horizontal wind vector difference between two adjacent height levels:

https://doi.org/10.5194/egusphere-2026-1739
Preprint. Discussion started: 20 May 2026

$$S = \frac{(\Delta u^2 + \Delta v^2)^{0.5}}{\Delta z} \quad (2)$$

where the vector difference between the horizontal wind at two altitudes is normalized by the vertical distance (Δz) between them.

2.3 The identification of LLJs

Building upon the classification schemes in our previous work (Wei et al., 2025b), we identify LLJ events in Hefei based on the following objective criteria: (1) The maximum wind speed (V_{max}) in the lower troposphere must reach or exceed 8 m s^{-1}; (2) A distinct jet core must be present, defined by a significant wind speed decrease of at least 4 m s^{-1} ($\Delta V = V_{max} - V_{min}$) between the jet core and the first local minimum (V_{min}) above it; (3) The LLJ core height is determined by the altitude of V_{max}. In cases where multiple wind speed maxima occur simultaneously at different levels, the lowest jet layer is prioritized as it exerts the most direct influence on surface pollution patterns. These thresholds are applied consistently to both events in order to ensure a comparable identification of LLJ structures across cases.

2.4 Meteorological and air quality data

The ambient air quality data (i.e., $PM_{2.5}$ and PM_{10} concentrations) are obtained from the National Real-Time Air Quality Reporting System of the China National Environmental Monitoring Center (CNEMC; http://www.cnemc.cn/, last access: 21 March 2026). This study utilizes city-wide average values from multiple monitoring stations in Hefei to represent regional pollution levels; specific locations for all sites are available on the official portal (https://aqicn.org/city/hefei/, last access: 21 March 2026). The nearest monitoring station to the CDWL system is located on Changjiang Middle Road (31.852°N, 117.25°E), approximately 2.7 km to the northwest. The surface meteorological data (i.e., air temperature and dew point temperature) are acquired from the National Meteorological Information Center (NMIC; http://www.nmic.cn/, last access: 21 March 2026). The ERA5 reanalysis data are used to characterize the synoptic conditions and the vertical thermal structure of the atmosphere (Hersbach et al., 2020). The dataset provides hourly estimates for numerous atmospheric, oceanic, and land-surface quantities on a 0.25°×0.25° regular latitude-longitude grid.

https://doi.org/10.5194/egusphere-2026-1739
Preprint. Discussion started: 20 May 2026

3 Cases overview and synoptic conditions

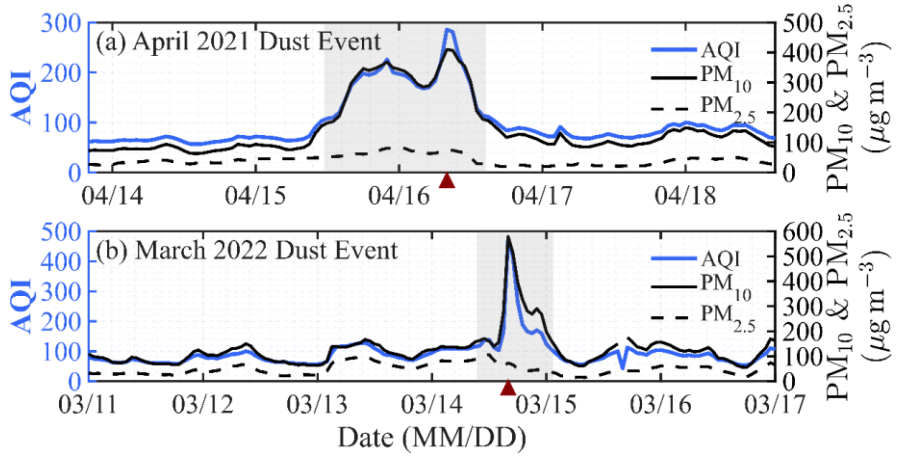

Figure 2. Time series of air quality parameters during the dust events in (a) April 2021 and (b) March 2022. The blue solid line represents the Air Quality Index (AQI), while the black solid and dashed lines denote PM_{10} and $PM_{2.5}$ concentrations (μg m^{-3}), respectively. The grey shaded areas indicate the identified dust event periods, and the red triangles mark the occurrence of the peak PM_{10} concentration.

According to the Atmospheric Environmental Meteorological Bulletin issued by the China Meteorological Administration (https://www.cma.gov.cn/zfxxgk/gknr/qxbg/, last access: 21 March 2026), the dust episode (No. 202107) from 14-16 April 2021 is classified as a dust storm. This episode is associated with the coupling of a Mongolian cyclone and a surface cold front. The dust originates in central Inner Mongolia and propagates southeastward, resulting in blowing or floating dust across central and northern Anhui Province. Preceding drought conditions that loosen the topsoil, combined with intensified near-surface winds, facilitate the emission and long-range dispersion of dust particles (Mai et al., 2021). Similarly, the dust episode (No. 202202) from 13-16 March 2022 reaches dust storm intensity. Under the combined forcing of a Mongolian cyclone and a cold front, dust plumes originate from central Inner Mongolia. As the plume moves eastward and southward, it affects central and northern Anhui, reducing air quality and horizontal visibility. This episode involves widespread dust activity across multiple northern provinces, impacting the regional atmospheric environment (Mai and Zhang, 2022).

Building upon the identification and preliminary aerosol characterization of these two episodes reported by Wang et al. (2024), the present study conducts a more detailed investigation into the underlying boundary layer dynamic drivers. Utilizing a $PM_{2.5}/PM_{10}$ ratio below 0.18 and an hourly PM_{10} concentration exceeding 150 μg m^{-3} as identification criteria, the two dust episodes (Fig. 2) are defined from 11:00 LT on 16 April to 14:00 LT on 17 April 2021 (April 2021 event), and from 09:00 LT on 14 March to 01:00 LT on 15 March 2022 (March 2022 event). While previous work focused on the general aerosol properties, the current analysis examines the specific role of the LLJ in influencing aerosol vertical distribution. Specifically, the focus is on how the evolution of vertical wind structures and atmospheric stability relate to the distinct surface pollution patterns observed in these two dust episodes.

https://doi.org/10.5194/egusphere-2026-1739
Preprint. Discussion started: 20 May 2026

3.1 The April 2021 dust event

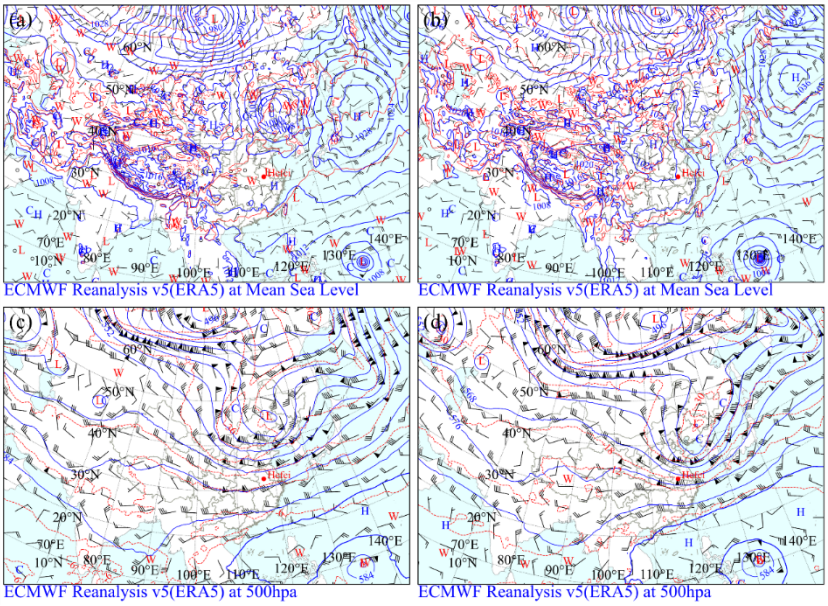

Figure 3. Synoptic weather patterns for the April 2021 dust event: (a) surface weather map at 00:00 UTC, 16 April 2021; (b) surface weather map at 00:00 UTC, 17 April 2021; (c) 500 hPa geopotential height (blue lines, gpm), isotherms (red lines, °C), and wind barbs at 00:00 UTC, 16 April 2021; (d) same as (c) but for 17 April 2021. The blue letters "L" and "C" indicate low-pressure and cold centers, respectively; the red letters "H" and "W" indicate high-pressure and warm centers.

Preceding the April 2021 event, the dust source regions in northern China and Mongolia experience a notably warm spring, with temperatures 1.1 °C above the climatological mean. This prolonged warming, coupled with a significant precipitation deficit in April (less than 10 mm in parts of Inner Mongolia), leads to the desiccation of the topsoil. Dynamically, the synergistic influence of a deep Mongolian Cyclone and a Northeast Cold Vortex (Figs. 3a-b) provides the primary driving force for large-scale dust emission and the long-range transport. At mean sea level, the cyclone deepens during its eastward propagation, accompanied by strong northwesterly winds. At 500 hPa (Figs. 3c-d), the deepening cold vortex guides polar cold air southward, overlapping with the low-level cold advection. The presence of an 850 hPa warm ridge beneath 500 hPa cold advection creates a thermodynamic instability (warm-below and cold-above), which facilitates turbulent mixing. This synoptic forcing corresponds to the air quality profile observed in Hefei (Fig. 2a). As the cold front passes, the surface PM_{10} concentration exhibits a multi-peak pattern, increasing from background levels to a maximum of 410 μg m^{-3} at 08:00 LT on 17 April 2021. This intrusion is characterized by a rapid response to the downward transfer of high-level momentum and dust particles, reflecting an unstable boundary layer where strong synoptic-scale forcing dominates local stratification.

https://doi.org/10.5194/egusphere-2026-1739
Preprint. Discussion started: 20 May 2026

3.2 The March 2022 dust event

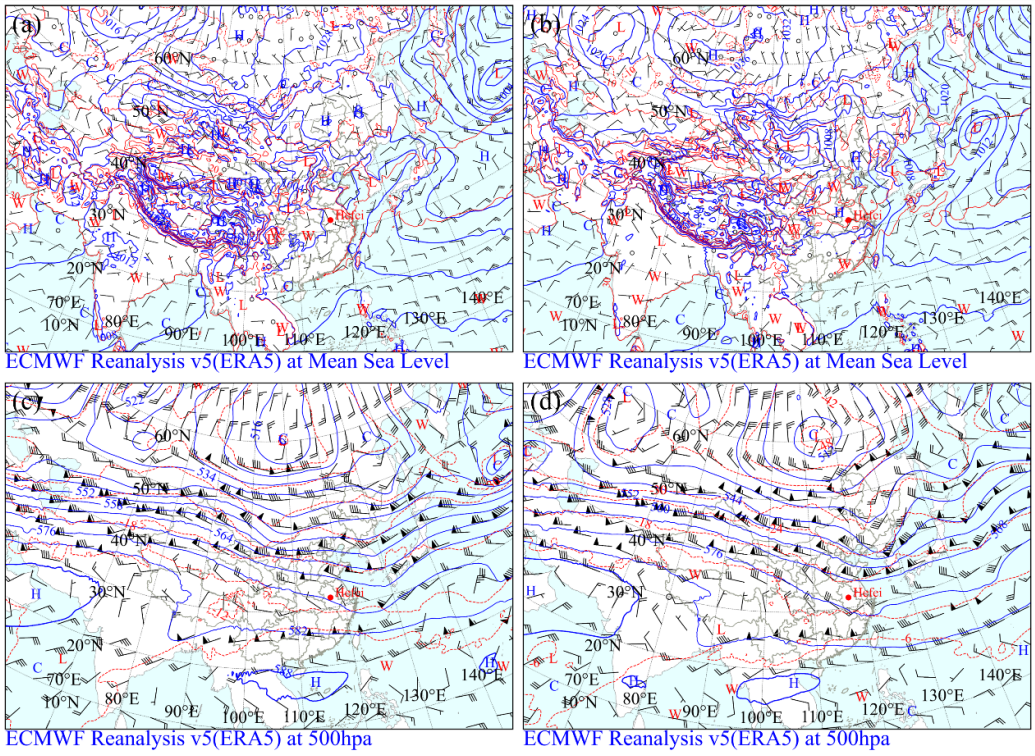

Figure 4. Synoptic weather patterns for the March 2022 dust event: (a) surface weather map at 08:00 UTC on 13 March 2022; (b) surface weather map at 08:00 UTC on 14 March 2022; (c) 500 hPa weather map at 08:00 UTC on 13 March 2022; (d) 500 hPa weather map at 08:00 UTC on 14 March 2022. Notation follows Fig.3.

The March 2022 event exhibits different circulation characteristics. Although spring 2022 also experiences record-high temperatures, a 25% increase in March precipitation over the dust source regions enhances soil moisture and inhibits dust deflation. Furthermore, a weaker polar vortex and a shallower East Asian Trough restrict the intensification of the Mongolian Cyclone (Figs. 4a-b), resulting in weaker surface dynamic forcing compared to the previous year. At 500 hPa (Figs. 4c-d), the primary driver is a southward-extending East Asian Trough. The northwesterly jet behind this trough provides sustained momentum for the southward advection of dust particles. The subsidence and dry air masses associated with the rear of the trough favor the long-range transport and gradual deposition of dust in downstream regions. Correspondingly, the surface air quality in Hefei (Fig. 2b) exhibits a single, pronounced PM_{10} peak (578 μg m^{-3}) at 16:00 LT on 15 March 2022. Despite the weaker surface pressure gradient, the stable upper-level trough-driven transport allows dust to be advected within an elevated layer. The sudden surface peak occurs under relatively stable synoptic conditions, suggesting that the pollution maximum is not exclusively a result of frontal passage but is likely associated with localized boundary-layer dynamics, including LLJ-related downward redistribution. These contrasting synoptic configurations, which are characterized by the unstable intrusion in 2021 and the advection-dominant transport in 2022, provide the background for

https://doi.org/10.5194/egusphere-2026-1739
Preprint. Discussion started: 20 May 2026

the distinct LLJ behaviors. Their subsequent impacts on aerosol particle redistribution are further analyzed using lidar observations in the following sections.

4 Results

4.1 Vertical evolution of meteorological fields and inversion structure

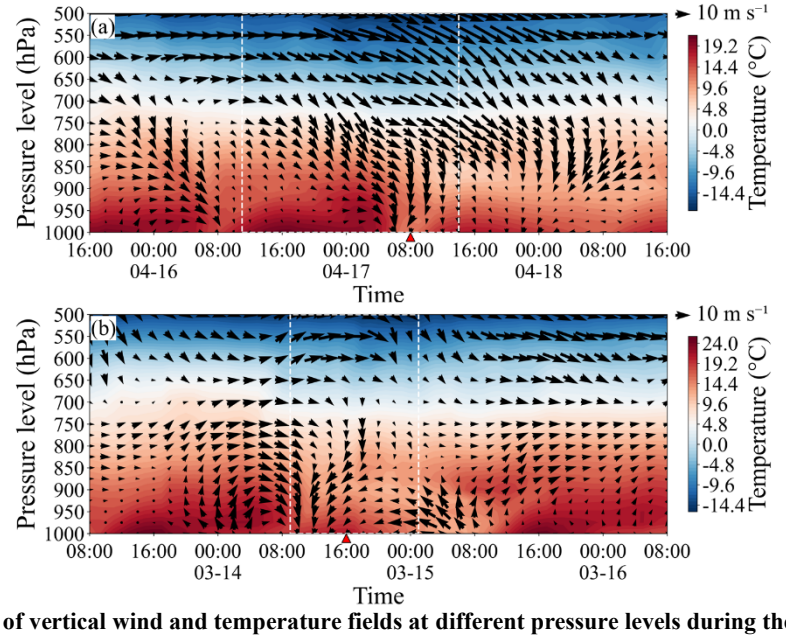

Figure 5. Hourly evolution of vertical wind and temperature fields at different pressure levels during the dust events. Black arrows represent horizontal wind vectors (upward direction indicates North). White dashed boxes denote the duration of the dust episodes, and red triangles mark the timing of the peak PM_{10} concentration. (a) 15-18 April 2021; (b) 13-16 March 2022. All data are retrieved from the ERA5 hourly reanalysis datasets (0.25°×0.25°).

Figure 5 illustrates the hourly vertical evolution of the wind and temperature fields at the Hefei site which are derived from the ERA5 hourly reanalysis datasets. In the April 2021 event (Fig. 5a), a prominent warm air mass occupies the lower troposphere (below 900 hPa) before 06:00 LT on 17 April. The isotherms (Fig. A1a) show a significant downward compression of the 20 °C line toward the surface, reflecting an intensified vertical thermal gradient and characteristic pre-frontal warming. This elevated warmth, coupled with nocturnal radiative cooling at the surface, maintains a shallow inversion layer below 950 hPa between 05:00 and 09:00 LT (Fig. A2a). After 06:00 LT, this warm zone is abruptly truncated by the advancing leading edge of the cold front, marked by a sharp temperature drop and downward-slanting wind vectors. This thermal transition signifies a dynamic dust intrusion, during which the corresponding surface PM_{10} and AQI increase significantly (Fig. 2a). Moreover, this process is accompanied by a rapid intensification of northwesterly winds aloft and northerly winds near the surface. The resulting cold advection leads to a substantial temperature decline of ~9 °C, coinciding with the surface PM_{10} peak at 08:00 LT.

https://doi.org/10.5194/egusphere-2026-1739
Preprint. Discussion started: 20 May 2026

In contrast, the March 2022 event (Fig. 5b) exhibits a less significant temperature decline prior to the PM_{10} peak (16:00 LT, 15 March). During this period, the low-level wind field displays a distinct orientation, characterized by northeasterly or northerly winds, which contrasts with the northwesterly flow observed above 700 hPa. This vertical wind direction shear, coupled with a minimum wind speed zone near 750 hPa, indicates a decoupling between the boundary layer and the free atmosphere. Notably, a persistent capping inversion is maintained at 900-875 hPa from the beginning of the dust episode through the early afternoon (Fig. A2b). This stable stratification is consistent with the isotherm distribution in Fig. A1b, where the isotherms are densely layered below 900 hPa and become sparse in the overlying layer (900-800 hPa). This vertical gradient suggests thermal decoupling, where the near-surface stability restricts vertical exchange and maintains aerosols above the inversion base. This configuration distinguishes the event from the rapid dynamic forcing observed in 2021.

4.2 Co-evolution of LLJ and aerosol vertical distribution

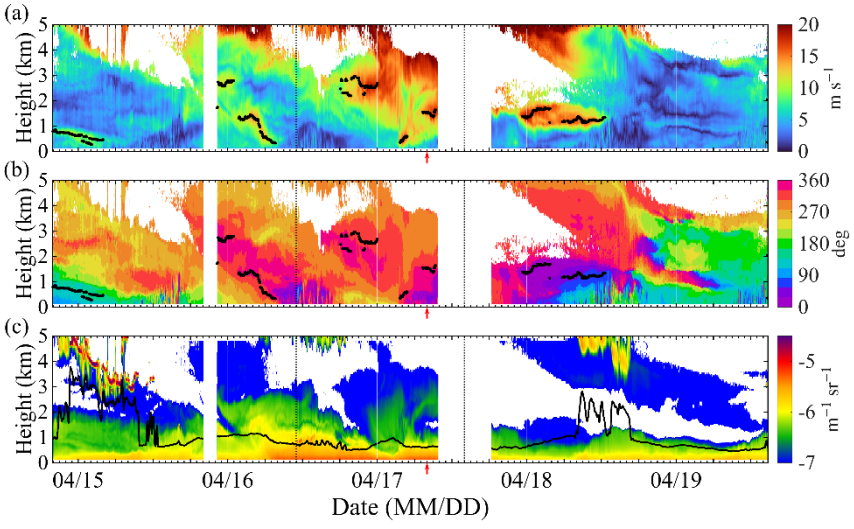

Figure 6. Lidar observations from 20:00 on 14 April to 15:00 local time on 19 April 2021: (a) horizontal wind speed (m s^{-1}); (b) horizontal wind direction (deg, where 0° represents North); (c) logarithmic attenuated backscatter coefficient (log10 (m^{-1} sr^{-1})). Black dots in (a) and (b) denote the low-level jet core height (km); the thin black line in (c) indicates the aerosol backscatter centroid height (km). The red arrow indicates the timing of the PM_{10} peak concentration. The labels 'MM/DD' on the horizontal axis represent the month and day, respectively.

Figure 6 presents the time-height evolution of horizontal wind speed, wind direction, and the logarithmic attenuated backscatter coefficient (β) during the April 2021 event. The backscatter centroid height is used to characterize the vertical distribution of the aerosol loading and is defined as the altitude-weighted average of backscatter from 0 to 5 km. The vertical extent of the aerosol loading is further quantified by the aerosol layer top (ALT), which is defined as the lowest altitude where the backscatter intensity drops below a threshold of 10^{-6} m^{-1} sr^{-1}.

https://doi.org/10.5194/egusphere-2026-1739
Preprint. Discussion started: 20 May 2026

Observations from pre-event stage (15-16 April) establish the baseline boundary-layer conditions prior to the dust transport. Prior to the dust intrusion (15 April), the lower atmosphere is characterized by a persistent southeasterly boundary-layer jet (BLJ, > 8.4 m s^{-1}) below 1 km. During this period, the backscatter intensity remains weak, indicating a clean background with low local aerosol loading. By the early hours of 16 April, the transition to a synoptic-system-related LLJ (SLLJ) with northwesterly winds (> 10.7 m s^{-1}) indicates the approach of the cold frontal system. As the jet core descends from 2.7 km to 0.3 km, the ALT increases from 0.4 km (04:00 LT) to 1.5 km (06:00 LT), indicating the initial vertical transport and inflow of upstream dust. Subsequently, the broadly synchronous descent of the ALT and centroid height suggests that aerosols remain concentrated within the descending jet layer and have not yet reached the near-surface layer in high concentrations.

During the dust influence stage (11:00 LT 16 April to 14:00 LT 17 April), an intensified cold air surge is associated with the development of an SLLJ with speeds of 15.5 m s^{-1} (18:00 to 00:00 LT). Initially situated at a mean core height of 2.5 km, the jet core descends sharply to 0.5 km by 03:30 LT with speeds exceeding 13.4 m s^{-1} on 17 April. Approximately 30 minutes before the jet core reaches 0.3 km, ALT begins to rise, reaching 0.7 km as the jet dissipates. This height fluctuates around the period of the surface PM_{10} peak, suggesting that jet-induced wind shear and associated turbulent mixing may facilitate the downward redistribution of dust. The low background concentrations on 15 April and the progressive downward migration of dust particles on 16 April suggest that the surface peak on 17 April is associated with intensified downward dynamical forcing.

In the post-event stage, a final SLLJ (23:00 LT on 17 April to 03:45 LT on 18 April) with a mean core height of 1.5 km and speeds exceeding 15.8 m s^{-1} continues to modulate the aerosol vertical structure. High backscatter values (> $10^{-6.5}$ m^{-1} sr^{-1}) descend to 0.5 km following the jet's maximum height. The eventual shift to northeasterly winds and the decrease in ALT indicates the removal of the dust layer and the restoration of typical atmospheric conditions.

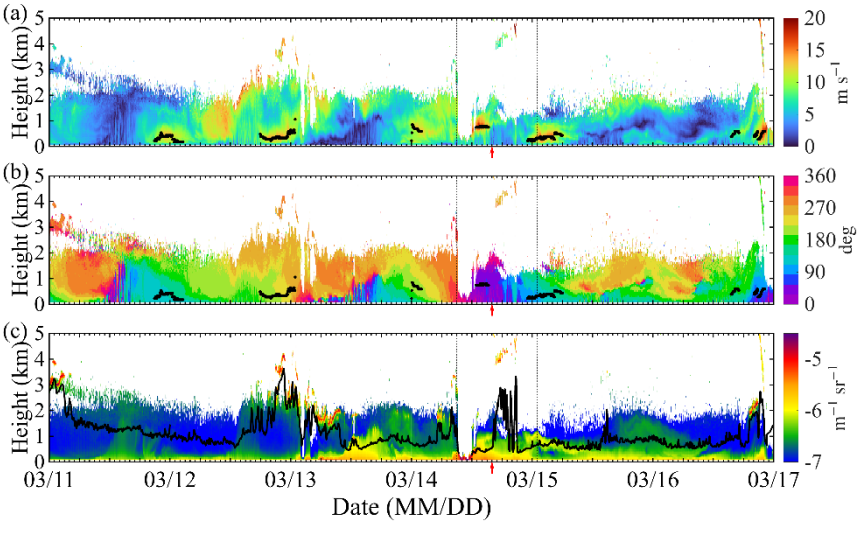

Figure 7. Lidar observations from 00:00 on 11 March to 00:00 local time on 17 March 2022. Notation follows Fig.6.

https://doi.org/10.5194/egusphere-2026-1739
Preprint. Discussion started: 20 May 2026

Prior to the dust intrusion (12-13 March), the lower atmosphere is characterized by alternating LLJ regimes. From 18:00 LT on 12 March to 01:00 LT on 13 March, a southwesterly LLJ (> 10.9 m s^{-1}) is observed with a mean core height of 0.4 km (Figs. 7a-b). Unlike the 2021 case where the northwesterly LLJ triggers dust entrainment, this southwesterly jet acts to stabilize the lower atmosphere, keeping the ALT at its minimum range (< 0.1 km). Following the dissipation of this jet and a subsequent shift to northwesterly winds, the ALT gradually ascends to 1.0 km by 12:00 LT on the 13th, marking a significant vertical expansion. By 17:37 LT, the near-surface wind shifts to southeasterly and the ALT drops below 0.1 km, reflecting the suppression of vertical mixing after sunset. On the early morning of 14 March, a brief southwesterly LLJ (> 10.6 m s^{-1}) with a mean core height of 0.7 km transiently stabilizes the nocturnal layer, maintaining a low ALT. The onset of daytime convective mixing and a shift to northwesterly winds by 08:00 LT lead to a rapid rise in ALT, preceding the main dust intrusion.

The main phase of the dust intrusion (09:00 LT 14 March to 01:00 LT 15 March) exhibits a predominantly horizontal transport mode. A strong northwesterly LLJ (> 12.1 m s^{-1}) with a relatively stable core height of approximately 0.7 km shows high vertical consistency with the ALT peak. In contrast to the descending jet observed in April 2021, the March 2022 event maintains a near-constant altitude, reflecting transport within a stratified layer. As the LLJ weakens after 15:00 LT, the ALT decreases, followed by the surface PM_{10} peak.

During the waning phase (after 01:00 LT 15 March), a shallow LLJ with a mean core height of 0.3 km accompanies the final attenuation of the dust layer. A relatively low-backscatter zone (< $10^{-6.5}$ m^{-1} sr^{-1}) at 0.5 km slowly subsides to 0.3 km until the jet disappears after 06:00 LT, indicating the restoration of typical atmospheric conditions.

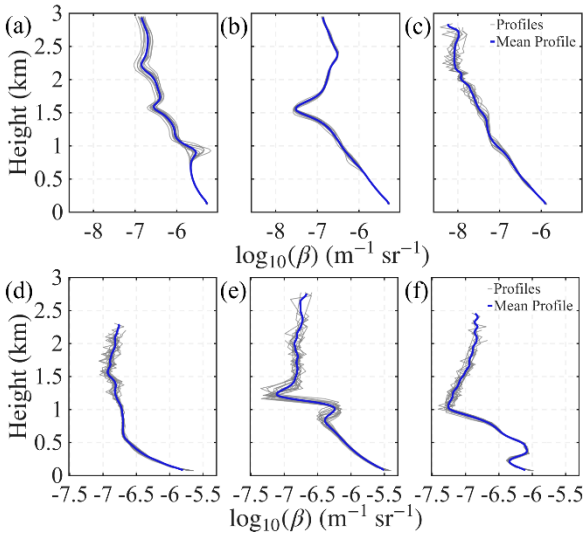

Figure 8. Vertical profiles of the logarithmic attenuated backscatter coefficient ($log_{10}(m^{-1}\ sr^{-1})$) before (a, d), during (b, e), and after (c, f) the PM_{10} peak for the 2021 (top) and 2022 (bottom) events. Grey lines represent 3-minute actual profiles; blue lines represent 30-minute mean profiles.

https://doi.org/10.5194/egusphere-2026-1739
Preprint. Discussion started: 20 May 2026

To further quantify the vertical structure, β profiles are analyzed across three stages: pre-peak, during-peak, and post-peak. The during-peak stage is defined as a 30-minute window centered on the PM_{10} peak, while the pre- and post-peak stages are selected at equivalent time intervals to ensure comparability. Fig. 8 illustrates the 3-minute instantaneous profiles (grey) alongside the 30-minute means (blue) to assess structural variability.

In the April 2021 event, the profiles exhibit distinct stage-wise transitions. Across all stages, the near-surface signals remain relatively stable with minimal standard deviation (SD < 0.01). During the pre-peak stage (Fig. 8a), β decreases with altitude in an oscillatory pattern, with values exceeding $10^{-5.5}$ m^{-1} sr^{-1} below 0.33 km and reaching a minimum of $10^{-6.8}$ m^{-1} sr^{-1} at 2.93 km. A localized low-value zone (<$10^{-6.5}$ m^{-1} sr^{-1}) is identified between 1.54 and 1.63 km, which is consistent with the layered structure in the time-height sections. A variance maximum (SD = 0.18) at 0.93 km indicates a layer of increased signal volatility. During the peak stage (Fig. 8b), the most significant transition of vertical β gradient occurs, which is characterized by a decreasing-then-increasing trend as altitude increases. Notably, the vertical gradient of β is -1.27×10^{-3} m^{-1} sr^{-1} below 1.30 km and reaches -3.23×10^{-3} m^{-1} sr^{-1} between 1.30 and 1.54 km, indicating a sharp concentration gradient. During the post-peak stage (Fig. 8c), β profiles show a general decreasing trend with altitude with a mean gradient of -1.34×10^{-3} m^{-1} sr^{-1} below 1 km. β above 0.69 km decreases by approximately one order of magnitude relative to the pre-peak levels.

The March 2022 event exhibits a more complex evolution of β profiles than the April 2021 event, characterized by multi-layered vertical transitions and structural reconfigurations across. During the pre-peak stage (Fig. 8d), β declines from $10^{-5.7}$ to $10^{-6.7}$ m^{-1} sr^{-1} within the 0.09-0.69 km layer. Subsequently, the profile nearly maintains relatively constant with a slight increase up to approximately 1.57 km ($10^{-6.9}$ m^{-1} sr^{-1}). During the peak stage (Fig. 8e), the vertical structure complexity increases. Below 0.84 km, β decreases from $10^{-5.4}$ to $10^{-6.4}$ m^{-1} sr^{-1}, and then increases to a secondary peak of $10^{-6.2}$ m^{-1} sr^{-1} at 1.06 km. This is followed by a sharp decline to a minimum ($10^{-7.1}$ m^{-1} sr^{-1}) at 1.21 km, after which the signal increases again. This fluctuating pattern below 1.5 km represents a more stratified dust layer compared to the 2021 peak. During the post-peak stage (Fig. 8f), β first decreases from $10^{-6.0}$ to $10^{-6.3}$ m^{-1} sr^{-1} (0.09-0.21 km), then recovers to $10^{-6.0}$ m^{-1} sr^{-1} at 0.36 km, followed by a decline to its absolute minimum of $10^{-7.2}$ m^{-1} sr^{-1} at 1.03 km. Finally, the profile increases once more within a relatively low-value zone (<$10^{-7.0}$ m^{-1} sr^{-1}) between 0.93 and 1.57 km. This pattern indicates a substantial structural reconfiguration during the waning phase.

https://doi.org/10.5194/egusphere-2026-1739
Preprint. Discussion started: 20 May 2026

4.3 Impact of LLJs on the vertical characteristics of wind shear and turbulence

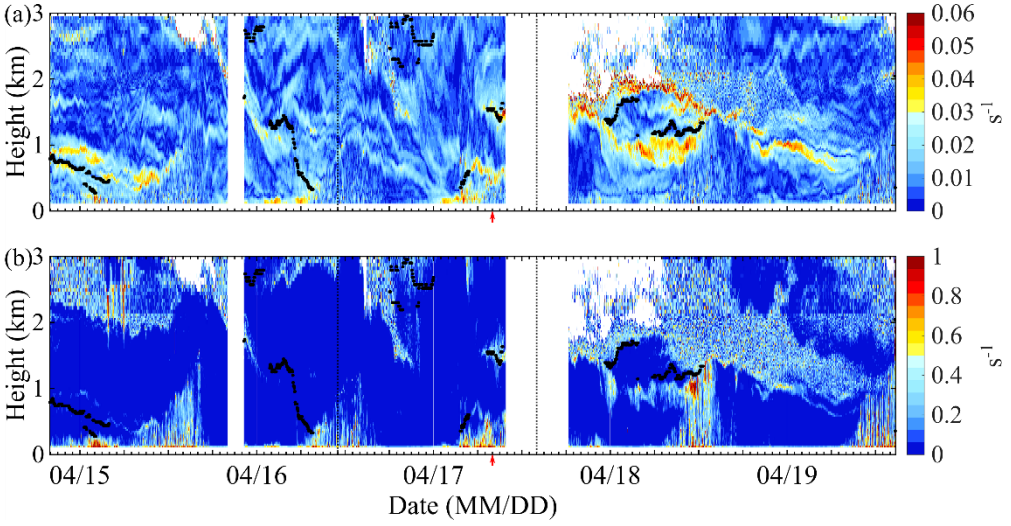

Figure 9. Lidar observations from 20:00 LT on April 14 to 15:00 LT on April 19, 2021: (a) vertical wind shear (s^{-1}), and (b) spectral width (s^{-1}). Black dots indicate the LLJ nose height, and red arrows represent the time of peak PM_{10} concentration. The labels 'MM/DD' on the horizontal axis represent the month and day, respectively.

Figure 9 presents the vertical wind shear (s^{-1}) and spectral width (s^{-1}) retrieved from the Doppler wind lidar during the April 2021 event. Significant wind shear zones (WSZ, > 0.02 s^{-1}) and spectral width zones (SWZ, > 0.2 s^{-1}) are analyzed to characterize the relationship between LLJ evolution and turbulence intensity.

Prior to the dust intrusion, the lower troposphere is characterized by typical diurnal boundary layer evolution. On April 15, daytime convective mixing dominates, with the SWZ expanding to 1.5 km and reflecting a corresponding increase in ALT. On April 16, a high-level LLJ (2.7 km) descends and attenuates near 0.3 km by 07:38 LT, leading to short-term dynamic responses including near-surface vertical wind shear exceeding 0.04 s^{-1}. These observations of thermal-driven turbulence, characterized by the SWZ reaching approximately 1.1 km at 14:00 LT before decreasing, provide a representative baseline of typical boundary-layer conditions. This background helps to distinguish the subsequent mechanical forcing and its impact on aerosol distribution observed during the dust intrusion.

During the influence stage on April 17, a SLLJ descends from 2.5 km to 0.5 km within three hours. Notably, the WSZ ascends from 0.2 km to 1.0 km prior to the jet's descent, with strong near-surface wind shear (> 0.04 s^{-1}) appearing at 0.2 km as the jet core reaches 1.0 km. Furthermore, the SWZ expands upward from the surface after the jet core descends to 0.5 km, reaching a maximum height of 0.4 km at 07:30 LT, approximately 30 minutes before the surface PM_{10} peak. This temporal sequence suggests that LLJ-induced mechanical turbulence may contribute to the vertical mixing of dust aerosols and their subsequent transport toward the surface. However, the presence of a residual LLJ at 1.5 km late in the event coincides with low backscatter coefficients (< 10^{-7} m^{-1} sr^{-1}), suggesting that dynamic disturbances and aerosol distributions are not necessarily vertically synchronized.

https://doi.org/10.5194/egusphere-2026-1739
Preprint. Discussion started: 20 May 2026

In the post-case stage, the LLJ reappears at 1.5 km, rising to 1.7 km and influencing the vertical turbulence structure. As the jet core subsequently descends and dissipates at 1.3 km by 12:38 LT, large spectral width values (> 0.8 s^{-1}) at 1.0 km mark the final stage of jet-induced instability. Following the dissipation, the re-establishment of the WSZ at 1.5 km and the decline of the SWZ toward the surface by 15:00 LT indicate the restoration of typical diurnal boundary-layer characteristics, as the atmosphere returns to a state independent of significant LLJ constraints.

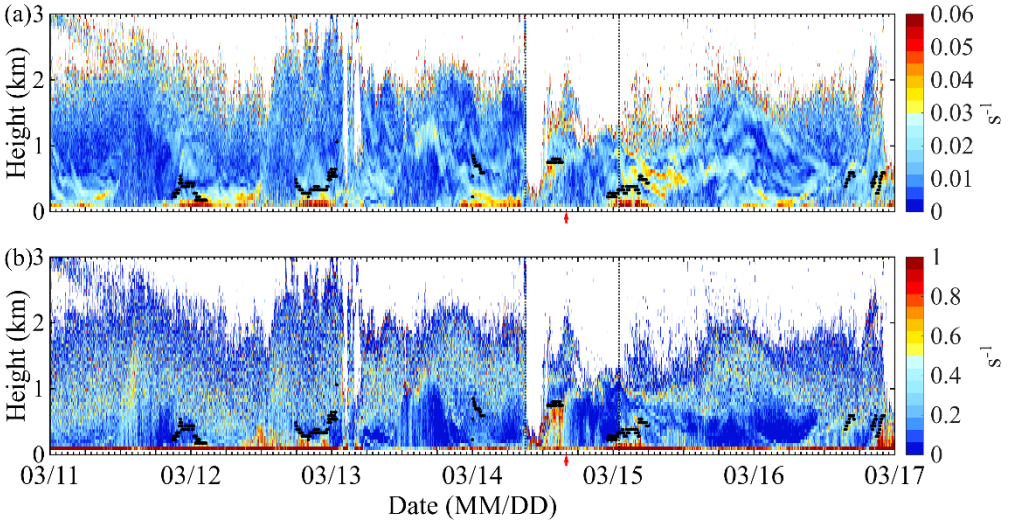

Figure 10. Lidar observations from 00:00 local time on 11 March to 00:00 local time on 17 March 2022. Notation follows Fig. 9.

Figure 10 illustrates the vertical wind shear and spectral width for the March 2022 event. To provide a meteorological reference, the pre-case stage (March 11-13) is briefly analyzed, showing a succession of LLJ activities with core heights between 0.2 and 0.4 km. These recurrent jets maintain an active turbulence environment, where the SWZ frequently extends to altitudes below 0.5 km. This background of persistent vertical mixing contrasts with the more stable pre-event conditions in April 2021.

On March 14, an initial LLJ is observed from 00:00 to 02:00 LT with an average core height of 0.7 km. Approximately 30 minutes before it appears, the WSZ height ascends from the near-surface to 0.4 km and maintains a height of 0.3 km until 09:00 LT, even after the jet dissipates. During the dust impact stage, intense spectral width (> 0.8 s^{-1}) is observed at an altitude of 0.5 km, indicating active turbulence within this layer. Around 12:00 LT, a zone of strong wind shear exceeding 0.06 s^{-1} rises from below 0.5 km to 0.7 km and expands further upward. This vertical expansion reflects a deepening of the turbulence layer, likely driven by the combined effects of LLJ-induced mechanical shear and daytime thermal convection. As surface PM_{10} reaches its peak, the enhanced WSZ contracts toward the near-surface layer (< 0.5 km). Between 01:00 and 15:00 LT, recurrent LLJ activity is observed with an average core height at 0.7 km, characterized by substantial wind shear and spectral width below the jet core. This indicates a close correspondence between LLJ activity and the vertical evolution of dynamic and turbulence structures during the transport phase.

https://doi.org/10.5194/egusphere-2026-1739
Preprint. Discussion started: 20 May 2026

In the post-event stage, the reappearance of a shallow LLJ at 0.4 km is associated with a final redistribution of turbulence before the system returns to typical diurnal boundary-layer characteristics. Overall, the March 2022 event demonstrates a sustained advection-transport process. This contrasts with the rapid dynamic forcing of April 2021, suggesting that the higher frequency and structural persistence of the jets in 2022 contribute to a more prolonged surface pollution accumulation.

4.4 LLJ formation and its relationship with surface pollution peaks

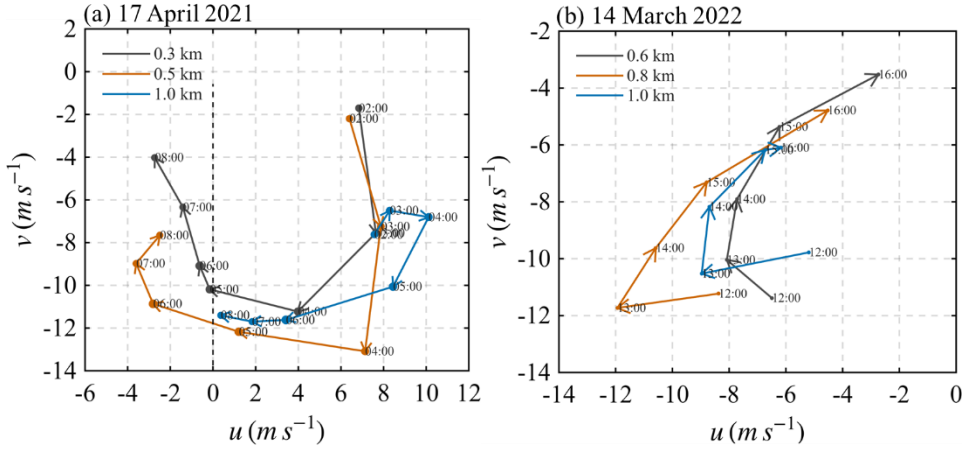

Figure 11. Hodographs of horizontal wind vectors (u, v) at representative altitudes during (a) the April 2021 event and (b) the March 2022 event. Numbers adjacent to the vectors denote the Local Time (LT).

The formation and evolution of LLJs play a critical role in modulating the vertical transport of aerosols and further influence surface pollution. To examine the underlying dynamical drivers, Figure 11 presents the wind hodographs (u, v components) during the periods immediately preceding and encompassing the PM_{10} peaks. Although these cases occur under strong synoptic forcing, the wind vectors at representative altitudes display a characteristic clockwise rotation during their respective peak-approaching phases. This feature suggests the presence of inertial oscillation (IO) signal, potentially amplified by the frontal system, which persists as a dynamical background after the boundary layer decouples from surface friction under stable stratification.

In the April event, the LLJ acts as a dynamic carrier of aerosols. Lidar observations (Fig. 6c) show that the β high-value zone exhibits an upward migration, tracking the ascent of the jet core from 0.3 to 1.0 km as it is lifted by the deepening cold air mass. While the surface temperature begins to decline, the relatively stable dew point until 08:00 LT (Fig. A3a) suggests that the peak PM_{10} occurs close to the frontal leading edge. Although the jet core migrates aloft, the vertical wind shear (Fig. 9a) at its lower interface (< 0.5 km) remains sufficiently intense to likely facilitate downward aerosol transport. This sustained shear may be linked to the observed IO signals (Fig. 11a). Given that these signals are more pronounced above the shallow inversion layer (Fig. A2a), the reduced frictional coupling allows for a distinct phase evolution of the wind vector,

https://doi.org/10.5194/egusphere-2026-1739
Preprint. Discussion started: 20 May 2026

which aligns with the intensified vertical wind shear. This dynamical configuration synchronizes with the initial approach of the cold front. While early cold advection enhances near-surface stability, the shallow depth of this post-frontal inversion (< 0.5 km) enables the shear-induced turbulence to maintain a connection between the ascending jet and the surface. The 08:00 LT PM_{10} peak coincides with a period of relatively favorable coupling within this evolving wind field, occurring before the jet core ascends beyond the layer of more effective surface-to-atmosphere exchange.

In the March event, the PM_{10} peak results from the vertical redistribution of a pre-accumulated aerosol layer. Unlike the April event, the surface peak at 16:00 LT occurs significantly after the initial frontal passage, as evidenced by the sharp dew point drop starting at 08:00 LT (Fig. A3b). This timing shift suggests that the event develops under a post-frontal cold-advective regime. The advancing cold air mass wedges beneath the ambient air, establishing a robust capping inversion layer between 900 and 875 hPa (Fig. A2b). Throughout the early afternoon, this inversion restricts vertical mixing, as indicated by the low-value gap in spectral width (12:00-15:00 LT, Fig. 10b), which leads to the accumulation of aerosols within the 0.5-1.0 km layer. It is noted that the cold-advective stratification coincides with the development of distinct IO signals above 0.6 km (Fig. 11b), reflecting the partial decoupling of the northerly flow (Fig. 7b) from surface friction. These signals act as dynamical indicators for the maintenance of both momentum and aerosols within the stable stratified layer. The peak at 16:00 LT coincides with the transient breakdown of the capping inversion and the downward redistribution of the previously elevated aerosol layer (Fig. 7c). This dynamic modulation may explain the delayed PM10 peak before the inversion re-establishes in the late evening (17:00–21:00 LT).

5 Discussion

The contrasting observations between the April 2021 and March 2022 episodes highlight two distinct physical regimes through which LLJ evolution is associated with aerosol vertical distribution. The 2021 case is consistent with the downward momentum-flux mechanism described in previous mineral dust studies (Knippertz and Todd, 2012; Fiedler et al., 2013), suggesting that the rapid downward migration of the SLLJ core helps overcome the shallow thermal stability established by cold-air wedging in this case. This dynamic-injection process is associated with intense wind shear at the jet's lower interface, which likely facilitates the transport of elevated dust into the near-surface layer and corresponds to the abrupt PM10 concentration increase. In contrast, the 2022 event reflects a stratified-transport regime, characterized by the presence of a robust capping inversion and a stable LLJ core. In this mode, the stable stratification limits vertical exchange, allowing aerosols to remain within an elevated layer during the horizontal advection process. This phenomenon is consistent with the barrier effect (Ren et al., 2022) often observed during persistent pollution stages, wherein the elevated aerosol layer remains decoupled from the surface until localized structural changes in the boundary layer are associated with gradual subsidence.

These results necessitate a re-evaluation of the timing of surface pollution peaks relative to synoptic forcing, particularly the phase lag between LLJ development and surface impact. While conventional analyses often attribute surface dust surges to the immediate passage of cold fronts or peak pressure gradients, the substantial 8-hour delay observed in the

https://doi.org/10.5194/egusphere-2026-1739
Preprint. Discussion started: 20 May 2026

2022 case demonstrates that the structural persistence of the LLJ and the associated stratification are more informative predictors of surface impact than surface wind speed alone. Unlike prior studies that predominantly rely on surface observations or low-resolution radiosondes, our use of high-resolution Doppler lidar observations effectively captures the fine-scale temporal evolution of the atmospheric boundary layer. The continuous profiles allow for tracking the shifting heights of the jet core alongside the aerosol layer, resolving the transition from elevated transport to downward mixing that is often overlooked by discrete sampling (Pichugina et al., 2017; Wang et al., 2026).

The dynamical foundation for the maintenance of these dust-bearing LLJs is further evidenced by the wind vector evolution in the hodographs, signifying the decoupling of the boundary layer from surface friction. Once decoupled, the wind vector undergoes the characteristic rotation associated with inertial oscillations (Blackadar, 1957), allowing the jet to maintain high speeds by reducing frictional dissipation and sustaining long-range advection. In the 2021 event, this dynamical shift aligns with the descent of the jet core, facilitating downward momentum transfer, whereas in the 2022 event, the persistence of this rotational pattern indicates a sustained decoupling phase that maintains the elevated dust layer. By resolving these profile-based dynamical backgrounds, this study suggests that the LLJ can act as an active modulator of vertical aerosol redistribution. This may help explain how downstream regions such as the Jiang-Huai Plain can experience severe pollution even after synoptic forcing weakens. This behavior differs from some previously reported cases in Beijing, where LLJs were associated with pollutant dilution (Miao et al., 2019). Such high-resolution insights are essential for improving current parameterization schemes in numerical models, which have been shown to underestimate LLJ strength and its corresponding impact on air quality (Sandu et al., 2013; Wei et al., 2023).

From a measurement perspective, this study also demonstrates the value of CDWL for resolving the coupled evolution of jet structure, wind shear, spectral width, and aerosol backscatter at event scale. The continuous high-resolution profiles provide information that cannot be captured by conventional surface observations or discrete soundings alone, particularly during short-lived transitions between elevated transport, downward mixing, and temporary aerosol storage. This observational capability is important for constraining boundary-layer processes in both numerical weather prediction and air quality applications.

6 Conclusions

This study investigates the contrasting roles of LLJ evolution in aerosol vertical redistribution during two dust episodes in Hefei, utilizing high-resolution Doppler wind lidar observations. The results suggest two distinct dynamical pathways. In the April 2021 event, the observations are consistent with a dynamic-injection process dominating the vertical dust transport. The northwesterly jet core exhibits a pronounced vertical migration, descending from 2.5 km to 0.3 km before re-ascending to around 1.0 km during the peak period, tracking the advancing cold front. This evolution generates intense wind shear exceeding 0.04 s^{-1} at the jet's lower interface, promoting mechanical turbulence that likely facilitates rapid downward dust transport. The backscatter profiles are consistent with this process, showing a sharp intensification of the vertical gradient

https://doi.org/10.5194/egusphere-2026-1739
Preprint. Discussion started: 20 May 2026

during the peak stage and supporting the interpretation of rapid dust injection into the boundary layer. Consequently, the surface PM_{10} peak (410 μg m^{-3}) exhibits little temporal delay relative to the frontal signal, as the shallow inversion layer appears to be mechanically overcome by jet-induced mixing during a period of favorable coupling before the jet core ascends beyond the layer of more effective exchange. In contrast, the March 2022 event represents a stratified-transport process. Here, the LLJ maintains a stable altitude (~0.7 km), while a persistent capping inversion (900-875 hPa) acts as a structural barrier, trapping aerosols within an elevated layer and decoupling them from the surface. Surface dew point and temperature traces indicate a post-frontal cold-advective process, under which the stable stratification maintains high backscatter intensities aloft during horizontal advection. The backscatter profiles exhibit a persistent multi-layered structure across the pre-peak and peak stages, further illustrating this vertical confinement. This configuration results in an approximately 8-hour phase lag between the surface frontal signal and the PM_{10} peak (578 μg m^{-3}). The peak occurs during the transient breakdown of the capping inversion, coinciding with the downward redistribution of the accumulated elevated aerosol layer.

The dynamical maintenance of these dust-bearing layers is associated with inertial oscillations, as evidenced by the characteristic clockwise rotation of wind vectors in hodographs after the boundary layer becomes decoupled from surface friction. By resolving fine-scale temporal transitions in vertical wind shear, spectral width, and aerosol backscatter, this study provides a comprehensive analysis of the diverse vertical transport mechanisms governed by the LLJ. These findings indicate that LLJ evolution can be associated with either aerosol injection into the boundary layer or elevated storage followed by delayed redistribution, depending on its height, intensity, and the specific stage of the pollution event. By providing direct observational evidence for these distinct transport mechanisms, this study establishes a process-level understanding that can help refine boundary-layer parameterizations in numerical models. Future work should leverage multi-site lidar networks to statistically validate the prevalence of these processes and assess their broader implications for regional air quality under varying synoptic conditions.

https://doi.org/10.5194/egusphere-2026-1739
Preprint. Discussion started: 20 May 2026

Appendix A

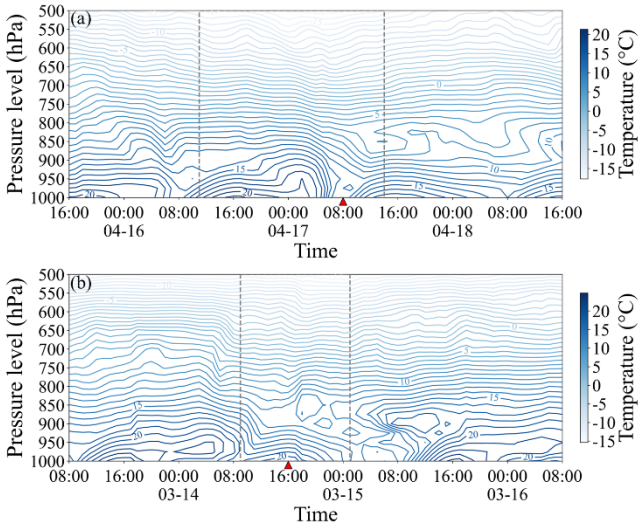

Figure A1. Time-pressure cross sections of temperature (isotherms) during the dust events. Gray dashed boxes denote the duration of the dust episodes, and red triangles mark the timing of the peak PM_{10} concentration. (a) 15-18 April 2021; (b) 13-16 March 2022. All data are retrieved from the ERA5 hourly reanalysis datasets (0.25°×0.25°).

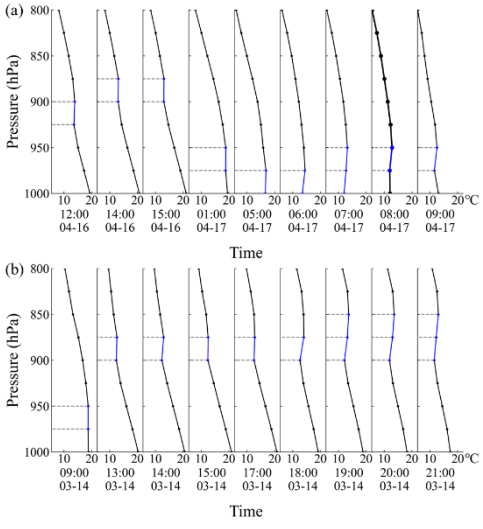

Figure A2. The evolution of temperature inversion layer during the dust events. (a) 16-17 April 2021; (b) 14 March 2022. All data are retrieved from the ERA5 hourly reanalysis datasets (0.25°×0.25°).

https://doi.org/10.5194/egusphere-2026-1739
Preprint. Discussion started: 20 May 2026

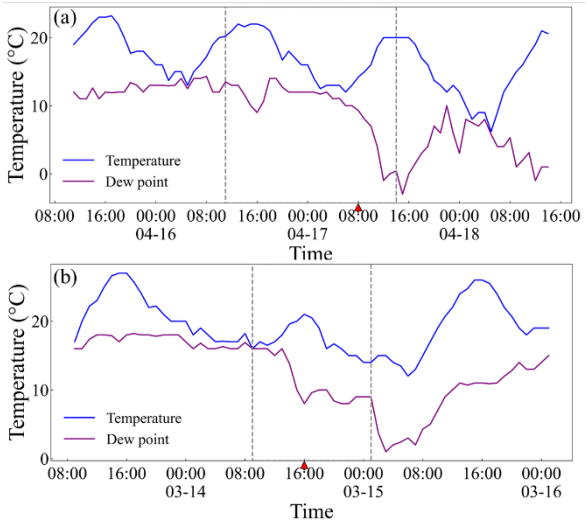

Figure A3. Hourly variations of surface air temperature and dew point temperature during the dust events. Gray dashed boxes denote the duration of the dust episodes, and red triangles mark the timing of the peak PM_{10} concentration. (a) 15-18 April 2021; (b) 13-16 March 2022. All data are extracted from meteorological station (ID: 58321) in Hefei city.

Code and data availability

No custom model code or dedicated analysis software was developed for this study. The Doppler wind lidar data used in this study are available from the corresponding author (Mengya Wang: wmengya123@nuist.edu.cn) upon reasonable request for non-commercial research purposes. The data include the processed wind profiles, attenuated backscatter coefficient, vertical wind shear, and spectral width for the two dust episodes analyzed in this study. The ERA5 reanalysis data are publicly available from the ECMWF Climate Data Store (https://cds.climate.copernicus.eu). Ambient air quality data are available from the China National Environmental Monitoring Center (CNEMC, http://www.cnemc.cn/). Surface meteorological data are available from the National Meteorological Information Center (NMIC, http://www.nmic.cn/).

Author contribution

Tianle Bai: Methodology, Data curation, Formal analysis, Visualization, Writing – original draft. Yuanyi Lin: Formal analysis, Visualization, Writing – original draft. Mengya Wang: Conceptualization, Methodology, Investigation, Writing – review & editing, Validation. Tianwen Wei: Methodology, Resources, Data curation. Fangzhi Wei: Resources, Data curation. Kuancheng Lv: Resources, Data curation. Haiyun Xia: Supervision, Resources, Validation.

Competing interests

The authors declare that they have no conflict of interest.

https://doi.org/10.5194/egusphere-2026-1739
Preprint. Discussion started: 20 May 2026

Acknowledgements

The authors thank the China National Environmental Monitoring Center (CNEMC) and the National Meteorological Information Center (NMIC) for providing the air quality and surface meteorological data used in this study. The authors are grateful to the ECMWF for making the ERA5 reanalysis datasets publicly available. We also acknowledge the support of the School of Atmospheric Physics, Nanjing University of Information Science and Technology, for providing the research infrastructure.

Financial support

This work was supported in part by the Project of the National Key Laboratory of Climate System Prediction and Change Response (CPRM-2025-NUIST-012).

References

Andújar-Maqueda, J., Ortiz-Amezcua, P., Demoz, B., Roots, M., Abril-Gago, J., Pandey, S., Pérez-Ramírez, D., Alados-Arboledas, L., and Guerrero-Rascado, J. L.: Doppler lidar observations of low-level jets and wind maxima over urban complex terrain in the southeastern Iberian Peninsula, Urban Clim., 65, 102744, https://doi.org/10.1016/j.uclim.2025.102744, 2026.

Banakh, V. A., Brewer, A., Pichugina, E. L., and Smalikho, I. N.: Measurements of wind velocity and direction with coherent Doppler lidar in conditions of a weak echo signal, Atmos. Oceanic Opt., 23, 381–388, https://doi.org/10.1134/S1024856010050076, 2010.

Banakh, V. A., Smalikho, I. N., and Falits, A. V.: Estimation of the turbulence energy dissipation rate in the atmospheric boundary layer from measurements of the radial wind velocity by micropulse coherent Doppler lidar, Opt. Express, 25, 22679–22692, 2017.

Banta, R. M., Newsom, R. K., Lundquist, J. K., Pichugina, Y. L., Coulter, R. L., and Mahrt, L.: Nocturnal low-level jet characteristics over Kansas during CASES-99, Boundary-Layer Meteorol., 105, 221–252, https://doi.org/10.1023/A:1019992330866, 2002.

Beu, C. M. L. and Landulfo, E.: Turbulence kinetic energy dissipation rate estimate for a low-level jet with Doppler lidar data: A case study, Earth Interact., 26, 112–121, https://doi.org/10.1175/EI-D-20-0027.1, 2022.

Chen, G., Wang, W.-C., and Chen, J.-P.: Circulation responses to regional aerosol climate forcing in summer over East Asia, Clim. Dyn., 51, 3973–3984, https://doi.org/10.1007/s00382-018-4267-3, 2018.

Dieudonné, E., Delbarre, H., Sokolov, A., Ebojie, F., Augustin, P., and Fourmentin, M.: Characteristics of the low-level jets observed over Dunkerque (North Sea French coast) using 4 years of wind lidar data, Q. J. R. Meteorol. Soc., 149, 1745–1768, https://doi.org/10.1002/qj.4480, 2023.

https://doi.org/10.5194/egusphere-2026-1739
Preprint. Discussion started: 20 May 2026

Frehlich, R.: Coherent Doppler lidar signal covariance including wind shear and wind turbulence, Appl. Opt., 33, 6472–6481, 1994.

Guo, J., Miao, Y., Zhang, Y., Liu, H., Li, Z., Zhang, W., He, J., Lou, M., Yan, Y., Bian, L., and Zhai, P.: The climatology of planetary boundary layer height in China derived from radiosonde and reanalysis data, Atmos. Chem. Phys., 16, 13309–13319, https://doi.org/10.5194/acp-16-13309-2016, 2016.

Gutierrez, W., Ruiz-Columbie, A., Tutkun, M., and Castillo, L.: Impacts of the low-level jet's negative wind shear on the wind turbine, Wind Energy Sci., 2, 533–545, https://doi.org/10.5194/wes-2-533-2017, 2017.

Heinold, B., Knippertz, P., and Beare, R. J.: Idealized large-eddy simulations of nocturnal low-level jets over subtropical desert regions and implications for dust-generating winds, Q. J. R. Meteorol. Soc., 141, 1740–1752, https://doi.org/10.1002/qj.2475, 2015.

Heinold, B., Knippertz, P., Marsham, J. H., Fiedler, S., Dixon, N. S., Schepanski, K., Laurent, B., and Tegen, I.: The role of deep convection and nocturnal low-level jets for dust emission in summertime West Africa: Estimates from convection-permitting simulations, J. Geophys. Res. Atmos., 118, 4385–4400, https://doi.org/10.1002/jgrd.50402, 2013.

Hersbach, H., Bell, B., Berrisford, P., Hirahara, S., Horányi, A., Muñoz-Sabater, J., Nicolas, J., Peubey, C., Radu, R., Schepers, D., Simmons, A., Soci, C., Abdalla, S., Abellan, X., Balsamo, G., Bechtold, P., Biavati, G., Bidlot, J., Bonavita, M., De Chiara, G., Dahlgren, P., Dee, D., Diamantakis, M., Dragani, R., Flemming, J., Forbes, R., Fuentes, M., Geer, A., Haimberger, L., Healy, S., Hogan, R. J., Hólm, E., Janisková, M., Keeley, S., Laloyaux, P., Lopez, P., Lupu, C., Radnoti, G., De Rosnay, P., Rozum, I., Vamborg, F., Villaume, S., and Thépaut, J.-N.: The ERA5 global reanalysis, Q. J. R. Meteorol. Soc., 146, 1999–2049, https://doi.org/10.1002/qj.3803, 2020.

Huang, T., Yang, Y., O'Connor, E. J., Lolli, S., Haywood, J., Osborne, M., Cheng, J. C. H., Guo, J., and Yim, S. H. L.: Influence of a weak typhoon on the vertical distribution of air pollution in Hong Kong: A perspective from a Doppler LiDAR network, Environ. Pollut., 276, 116534, https://doi.org/10.1016/j.envpol.2021.116534, 2021.

Huang, X., Ding, A., Wang, Z., Ding, K., Gao, J., Chai, F., and Fu, C.: Amplified transboundary transport of haze by aerosol–boundary layer interaction in China, Nat. Geosci., 13, 428–434, https://doi.org/10.1038/s41561-020-0583-4, 2020.

Iwai, H., Murayama, Y., Ishii, S., Mizutani, K., Ohno, Y., and Hashiguchi, T.: Strong updraft at a sea-breeze front and associated vertical transport of near-surface dense aerosol observed by Doppler lidar and ceilometer, Boundary-Layer Meteorol., 141, 117 – 142, https://doi.org/10.1007/s10546-011-9635-z, 2011.

Jia, M., Yuan, J., Wang, C., Xia, H., Wu, Y., Zhao, L., Wei, T., Wu, J., Wang, L., Gu, S. Y., Liu, L., Lu, D., Chen, R., Xue, X., and Dou, X.: Long-lived high-frequency gravity waves in the atmospheric boundary layer: Observations and simulations, Atmos. Chem. Phys., 19, 15431–15446, https://doi.org/10.5194/acp-19-15431-2019, 2019.

Knippertz, P. and Todd, M. C.: Mineral dust aerosols over the Sahara: Meteorological controls on emission and transport and implications for modeling, Rev. Geophys., 50, RG2007, https://doi.org/10.1029/2011RG000362, 2012.

https://doi.org/10.5194/egusphere-2026-1739
Preprint. Discussion started: 20 May 2026

Kok, J. F., Storelvmo, T., Karydis, V. A., Adebiyi, A. A., Mahowald, N. M., Evan, A. T., He, C., and Leung, D. M.: Mineral dust aerosol impacts on global climate and climate change, Nat. Rev. Earth Environ., 4, 71–86, https://doi.org/10.1038/s43017-022-00379-5, 2023.

Li, Z., Guo, J., Ding, A., Liao, H., Liu, J., Sun, Y., Wang, T., Xue, H., Zhang, H., and Zhu, B.: Aerosol and boundary-layer interactions and impact on air quality, Natl. Sci. Rev., 4, 810–833, https://doi.org/10.1093/nsr/nwx117, 2017.

Li, Z., Lau, W. K.-M., Ramanathan, V., Wu, G., Ding, Y., Manoj, M. G., Liu, J., Qian, Y., Li, J., Zhou, T., Fan, J., Rosenfeld, D., Ming, Y., Wang, Y., Huang, J., Wang, B., Xu, X., Lee, S.-S., Cribb, M., Zhang, F., Yang, X., Zhao, C., Takemura, T., Wang, K., Xia, X., Yin, Y., Zhang, H., Guo, J., Zhai, P. M., Sugimoto, N., Babu, S. S., and Brasseur, G. P.: Aerosol and monsoon climate interactions over Asia, Rev. Geophys., 54, 866–929, https://doi.org/10.1002/2015RG000500, 2016.

Li, Z., Wang, Y., Guo, J., Zhao, C., Cribb, M. C., Dong, X., Fan, J., Gong, D., Huang, J., Jiang, M., Jiang, Y., Lee, S.-S., Li, H., Li, J., Liu, J., Qian, Y., Rosenfeld, D., Shan, S., Sun, Y., Wang, H., Xin, J., Yan, X., Yang, X., Yang, X.-q., Zhang, F., and Zheng, Y.: East Asian study of tropospheric aerosols and their impact on regional clouds, precipitation, and climate (EAST-AIRCPC), J. Geophys. Res. Atmos., 124, 13026–13054, https://doi.org/10.1029/2019JD030758, 2019.

Mahrt, L.: Nocturnal boundary-layer regimes, Boundary-Layer Meteorol., 88, 255–278, https://doi.org/10.1023/A:1001171313493, 1998.

Mai, Z., Zhang, T., and Sheng, J.: Analysis of the April 2021 atmospheric circulation and weather (in Chinese), Meteorol. Mon., 47, 893–900, https://doi.org/10.7519/j.issn.1000-0526.2021.07.012, 2021.

Mai, Z. and Zhang, T.: Analysis of the March 2022 atmospheric circulation and weather (in Chinese), Meteorol. Mon., 48, 794–800, https://doi.org/10.7519/j.issn.1000-0526.2022.051001, 2022.

Miao, Y., Liu, S., Sheng, L., Huang, S., and Li, J.: Influence of boundary layer structure and low-level jet on PM2.5 pollution in Beijing: A case study, Int. J. Environ. Res. Public Health, 16, 616, https://doi.org/10.3390/ijerph16040616, 2019.

O'Connor, E. J., Illingworth, A. J., and Hogan, R. J.: A technique for autocalibration of cloud lidar, J. Atmos. Oceanic Technol., 21, 777–786, https://doi.org/10.1175/1520-0426(2004)021%3C0777:ATFAOC%3E2.0.CO;2, 2004.

Pentikäinen, P., O'Connor, E. J., Manninen, A. J., and Ortiz-Amezcua, P.: Methodology for deriving the telescope focus function and its uncertainty for a heterodyne pulsed Doppler lidar, Atmos. Meas. Tech., 13, 2849–2863, https://doi.org/10.5194/amt-13-2849-2020, 2020.

Pichugina, Y. L., Brewer, W. A., Banta, R. M., Choukulkar, A., Clack, C. T. M., Marquis, M. C., McCarty, B. J., Weickmann, A. M., Sandberg, S. P., Marchbanks, R. D., and Hardesty, R. M.: Properties of the offshore low level jet and rotor layer wind shear as measured by scanning Doppler lidar, Wind Energy, 20, 987–1002, https://doi.org/10.1002/we.2075, 2017.

Pöschl, U.: Atmospheric aerosols: Composition, transformation, climate and health effects, Angew. Chem. Int. Ed., 44, 7520–7540, https://doi.org/10.1002/anie.200501122, 2005.

https://doi.org/10.5194/egusphere-2026-1739
Preprint. Discussion started: 20 May 2026

Qin, K., Wu, L., Wong, M. S., Letu, H., Hu, M., Lang, H., Sheng, S., Teng, J., Xiao, X., and Yuan, L.: Trans-boundary aerosol transport during a winter haze episode in China revealed by ground-based lidar and CALIPSO satellite, Atmos. Environ., 141, 20–29, https://doi.org/10.1016/j.atmosenv.2016.06.042, 2016.

Ren, Y., Zhang, H., Zhang, X., Wu, B., Cai, X., Song, Y., and Zhu, T.: Quantitative verification of the turbulence barrier effect during heavy haze pollution events, Environ. Res. Commun., 4, 045005, https://doi.org/10.1088/2515-7620/ac6381, 2022.

Sandu, I., Beljaars, A., Bechtold, P., Mauritsen, T., and Balsamo, G.: Why is it so difficult to represent stably stratified conditions in numerical weather prediction (NWP) models?, J. Adv. Model. Earth Syst., 5, 117–133, https://doi.org/10.1002/jame.20013, 2013.

Smalikho, I.: Techniques of wind vector estimation from data measured with a scanning coherent Doppler lidar, J. Atmos. Oceanic Technol., 20, 276–291, https://doi.org/10.1175/1520-0426(2003)020%3C0276:TOWVEF%3E2.0.CO;2, 2003.

Stensrud, D. J.: Importance of low-level jets to climate: A review, J. Clim., 9, 1698–1711, https://doi.org/10.1175/1520-0442(1996)009%3C1698:IOLLJT%3E2.0.CO;2, 1996.

Fiedler, S., Schepanski, K., Heinold, B., Knippertz, P., and Tegen, I.: Climatology of nocturnal low-level jets over North Africa and implications for modeling mineral dust emission, J. Geophys. Res. Atmos., 118, 6100–6121, https://doi.org/10.1002/jgrd.50394, 2013.

Su, T., Li, Z., Li, C., Li, J., Han, W., Shen, C., Tan, W., Wei, J., and Guo, J.: The significant impact of aerosol vertical structure on lower atmosphere stability and its critical role in aerosol–planetary boundary layer (PBL) interactions, Atmos. Chem. Phys., 20, 3713–3724, https://doi.org/10.5194/acp-20-3713-2020, 2020.

Sullivan, J. T., Rabenhorst, S. D., Dreessen, J., McGee, T. J., Delgado, R., Twigg, L., and Sumnicht, G.: Lidar observations revealing transport of O3 in the presence of a nocturnal low-level jet: Regional implications for "next-day" pollution, Atmos. Environ., 158, 160–171, https://doi.org/10.1016/j.atmosenv.2017.03.039, 2017.

Tian, P., Cao, X., Zhang, L., Sun, N., Sun, L., Logan, T., Shi, J., Wang, Y., Ji, Y., Lin, Y., Huang, Z., Zhou, T., Shi, Y., and Zhang, R.: Aerosol vertical distribution and optical properties over China from long-term satellite and ground-based remote sensing, Atmos. Chem. Phys., 17, 2509–2523, https://doi.org/10.5194/acp-17-2509-2017, 2017.

Tuononen, M., O'Connor, E. J., Sinclair, V. A., and Vakkari, V.: Low-level jets over Utö, Finland, based on Doppler lidar observations, J. Appl. Meteorol. Climatol., 56, 2577–2594, https://doi.org/10.1175/JAMC-D-16-0411.1, 2017.

Wang, L., Liu, J., Gao, Z., Li, Y., Huang, M., Fan, S., Zhang, X., Yang, Y., Miao, S., Zou, H., Sun, Y., Chen, Y., and Yang, T.: Vertical observations of the atmospheric boundary layer structure over Beijing urban area during air pollution episodes, Atmos. Chem. Phys., 19, 6949–6967, https://doi.org/10.5194/acp-19-6949-2019, 2019.

Wang, M., Wei, T., Lolli, S., Rocadenbosch, F., Salcedo-Bosch, A., Du, Y., Wang, Y., Wang, C., Zong, L., Gu, Y., Wan, B., Su, L., Wei, F., and Xia, H.: A comparative study of low-level jets in different climate regions in China using multi-site Doppler wind lidar observations, IEEE Trans. Geosci. Remote Sens., https://doi.org/10.1109/TGRS.2026.3672972, 2026.

https://doi.org/10.5194/egusphere-2026-1739
Preprint. Discussion started: 20 May 2026

Wang, M., Wei, T., Lolli, S., Wu, K., Wang, Y., Hu, H., Yuan, J., Tang, D., and Xia, H.: A long-term Doppler wind LiDAR study of heavy pollution episodes in western Yangtze River Delta region, China, Atmos. Res., 310, 107616, https://doi.org/10.1016/j.atmosres.2024.107616, 2024.

Wang, Y., Li, B., Bao, P., Wang, R., Min, A., and Xiong, P.: A case study of leaf wettability variability and the relations with leaf traits and surface water storage for urban landscape plants, Water, 15, 2152, https://doi.org/10.3390/w15122152, 2023.

Wang, Y., Tang, J., Zhang, Z., Wang, W., Wang, J., and Wang, Z.: Hybrid methods' integration for remote sensing monitoring and process analysis of dust storm based on multi-source data, Atmosphere, 14, 3, https://doi.org/10.3390/atmos14010003, 2022.

Wei, T., Wang, M., Jiang, P., Wu, K., Zhang, Z., Yuan, J., Xia, H., and Lolli, S.: Retrieving aerosol backscatter coefficient using coherent Doppler wind lidar, Opt. Express, 33, 6832–6849, https://doi.org/10.1364/OE.551730, 2025a.

Wei, T., Wang, M., Wu, K., Yuan, J., Xia, H., and Lolli, S.: Characterizing urban planetary boundary layer dynamics using 3-year Doppler wind lidar measurements in a western Yangtze River delta city, China, Atmos. Meas. Tech., 18, 1841–1857, https://doi.org/10.5194/amt-18-1841-2025, 2025b.

Wei, T., Xia, H., Hu, J., Wang, C., Shangguan, M., Wang, L., Jia, M., and Dou, X.: Simultaneous wind and rainfall detection by power spectrum analysis using a VAD scanning coherent Doppler lidar, Opt. Express, 27, 31235–31245, 2019.

Wei, T., Xia, H., Wu, K., Yang, Y., Liu, Q., and Ding, W.: Dark/bright band of a melting layer detected by coherent Doppler lidar and micro rain radar, Opt. Express, 30, 3654–3663, https://doi.org/10.1364/OE.450714, 2022.

Wei, T., Xia, H., Wu, Y., Yuan, J., Wang, C., and Dou, X.: Inversion probability enhancement of all-fiber CDWL by noise modeling and robust fitting, Opt. Express, 28, 29662–29675, 2020.

Wei, W., Zhang, H., Zhang, X., and Che, H.: Low-level jets and their implications on air pollution: A review, Front. Environ. Sci., 10, 1082623, https://doi.org/10.3389/fenvs.2022.1082623, 2023.

Wu, B., Li, Z., Ju, T., and Zhang, H.: Characteristics of low-level jets during 2015–2016 and the effect on fog in Tianjin, Atmos. Res., 245, 105102, https://doi.org/10.1016/j.atmosres.2020.105102, 2020.

Yang, B., Finn, D., Rich, J., Gao, Z., and Liu, H.: Effects of low-level jets on near-surface turbulence and wind direction changes in the nocturnal boundary layer, J. Geophys. Res. Atmos., 128, e2022JD037657, https://doi.org/10.1029/2022JD037657, 2023.

Yang, Y., Yim, S. H. L., Haywood, J., Osborne, M., Chan, J. C. S., Zeng, Z., and Cheng, J. C. H.: Characteristics of heavy particulate matter pollution events over Hong Kong and their relationships with vertical wind profiles using high-time-resolution Doppler lidar measurements, J. Geophys. Res. Atmos., 124, 9609–9623, https://doi.org/10.1029/2019JD031140, 2019.

Yang, S., Preißler, J., Wiegner, M., von Löwis, S., Petersen, G. N., Parks, M. M., and Finger, D. C.: Monitoring dust events using Doppler lidar and ceilometer in Iceland, Atmosphere, 11, 1294, https://doi.org/10.3390/atmos11121294, 2020.

https://doi.org/10.5194/egusphere-2026-1739
Preprint. Discussion started: 20 May 2026

Zhang, K., Mao, H., Civerolo, K., Berman, S., Ku, J.-Y., Rao, S. T., Doddridge, B., Philbrick, C. R., and Clark, R.: Numerical investigation of boundary-layer evolution and nocturnal low-level jets: Local versus non-local PBL schemes, Environ. Fluid Mech., 1, 171–208, https://doi.org/10.1023/A:1011557402158, 2001.

Zhao, W. and Zou, Y.: Hefei: An emerging city in inland China, Cities, 77, 158–169, https://doi.org/10.1016/j.cities.2018.01.008, 2018.

Zheng, X. Y., Fu, Y. F., Yang, Y. J., and Liu, G. S.: Impact of atmospheric circulations on aerosol distributions in autumn over eastern China: Observational evidence, Atmos. Chem. Phys., 15, 12115–12138, https://doi.org/10.5194/acp-15-12115-2015, 2015.

Zhou, J., Yu, G., Jin, C., Qi, F., Liu, D., Hu, H., Gong, Z., Shi, G., Nakajima, T., and Takamura, T.: Lidar observations of Asian dust over Hefei, China, in spring 2000, J. Geophys. Res., 107(D15), https://doi.org/10.1029/2001JD000802, 2002.

Zhou, L., Liu, G., Shen, M., Liu, Y., and Lam, P. K. S.: Characteristics of indoor dust in an industrial city: Comparison with outdoor dust and atmospheric particulates, Chemosphere, 272, 129952, https://doi.org/10.1016/j.chemosphere.2021.129952, 2021.